

JGR Space Physics

RESEARCH ARTICLE

10.1029/2018JA026032

Key Points:

- A long-term data-model comparison of day-to-day thermospheric variability finds that GITM represents the weather poorly ($-0.07 < \rho < 0.36$)
- The average measured decorrelation time of 1.8 hr agrees with the modeled time of 1.9 hr
- The weather in GITM contains too little spatial structure, when compared with the measured $\sim 1,000$ -km decorrelation distance

Correspondence to:

B. J. Harding,
bhardin2@illinois.edu

Citation:

Harding, B. J., Ridley, A. J., & Makela, J. J. (2019). Thermospheric weather as observed by ground-based FPIs and modeled by GITM. *Journal of Geophysical Research: Space Physics*, 124, 1307–1316. <https://doi.org/10.1029/2018JA026032>

Received 24 AUG 2018

Accepted 10 JAN 2019

Accepted article online 19 JAN 2019

Published online 7 FEB 2019

Thermospheric Weather as Observed by Ground-Based FPIs and Modeled by GITM

Brian J. Harding¹ , Aaron J. Ridley² , and Jonathan J. Makela¹ 

¹Department of Electrical and Computer Engineering, University of Illinois at Urbana-Champaign, Urbana, IL, USA,

²Climate and Space Sciences and Engineering, University of Michigan, Ann Arbor, MI, USA

Abstract The first long-term comparison of day-to-day variability (i.e., weather) in the thermospheric winds between a first-principles model and data is presented. The definition of weather adopted here is the difference between daily observations and long-term averages at the same UT. A year-long run of the Global Ionosphere Thermosphere Model is evaluated against a nighttime neutral wind data set compiled from six Fabry-Perot interferometers at middle and low latitudes. First, the temporal persistence of quiet-time fluctuations above the background climate is evaluated, and the decorrelation time (the time lag at which the autocorrelation function drops to e^{-1}) is found to be in good agreement between the data (1.8 hr) and the model (1.9 hr). Next, comparisons between sites are made to determine the decorrelation distance (the distance at which the cross-correlation drops to e^{-1}). Larger Fabry-Perot interferometer networks are needed to conclusively determine the decorrelation distance, but the current data set suggests that it is $\sim 1,000$ km. In the model the decorrelation distance is much larger, indicating that the model results contain too little spatial structure. The measured decorrelation time and distance are useful to tune assimilative models and are notably shorter than the scales expected if tidal forcing were responsible for the variability, suggesting that some other source is dominating the weather. Finally, the model-data correlation is poor ($-0.07 < \rho < 0.36$), and the magnitude of the weather is underestimated in the model by 65%.

Plain Language Summary Much like in the lower atmosphere, weather in the upper atmosphere is harder to predict than climate. Physics-based models are becoming sophisticated enough that they can in principle predict the weather, and we present the first long-term evaluation of how well a particular model, Global Ionosphere Thermosphere Model, performs. To evaluate the model, we compare it with a year of data from six ground-based sites that measure the thermospheric wind. First, we calculate statistics of the weather, such as the decorrelation time, which characterizes how long weather fluctuations persist (1.8 hr in the data and 1.9 hr in the model). We also characterize the spatial decorrelation by comparing weather at different sites. The model predicts that the weather is much more widespread than the data indicates; sites that are 790 km apart have a measured correlation of 0.4, while the modeled correlation is 0.8. In terms of being able to actually predict a weather fluctuation on a particular day, the model performs poorly, with a correlation that is near zero at the low latitude sites, but reaches an average of 0.19 at the midlatitude sites, which are closer to the source that most likely dominates the weather: heating in the auroral zone.

1. Introduction

A critical barrier to prediction of the thermosphere-ionosphere system is an understanding of the day-to-day variability of the thermosphere, which we refer to as thermospheric weather. Recent advances in the development of first-principles numerical ionosphere-thermosphere models and specification of the lower and upper boundary variability have enabled the possibility of capturing the weather, and the recent expansion of ground-based wind networks has enabled the validation of these models.

While models are still not perfectly representing the climate, progress has been made, as reported in long-term model-data comparisons (Meriwether et al., 2013). In contrast, comparisons of the weather are largely confined to case studies. For example, Sutton et al. (2007) compared 8 days of cross-track wind estimates from the Challenging Minisatellite Payload with the thermosphere-ionosphere-electrodynamics general circulation model (TIEGCM), finding a mean absolute difference of 64.1 m/s, slightly better than

the comparison with the climatological Horizontal Wind Model 2014 (Drob et al., 2015). Wu et al. (2015) found that using the high-latitude variability prescribed by Super Dual Auroral Radar Network to drive the TIEGCM yielded better results than using the Heelis or Weimer models, in comparisons with ground-based wind measurements for a single storm period in December 2006. Wu et al. (2008) compared 10 days of TIEGCM runs from each of several years with ground-based wind observations in the polar cap, concluding that the TIEGCM overpredicted diurnal and semidiurnal oscillations. Emmert et al. (2001) developed an empirical model of daytime disturbance winds from Wind Imaging Interferometer data and compared it with the TIEGCM, finding important differences attributed mostly to high-latitude electric field variability. However, the Emmert et al. (2001) study averages data at a given local time, latitude, season, solar flux, and Kp, focusing on the effect of geomagnetic disturbances on the background circulation. This differs from true weather due to the influence of tidal variability and waves propagating from high latitudes.

In this paper we take a long-term approach to evaluating thermospheric weather, comparing a year-long run of the Global Ionosphere Thermosphere Model (GITM) with observations. We focus particularly on the wind because not only is it a critical parameter in thermosphere-ionosphere coupling, but it also offers an extensive ground-based data source, namely, networks of Fabry-Perot interferometers (FPIs). Previous studies have compared GITM to space-based observations (Deng & Ridley, 2006; Mehta et al., 2017), but in this study we utilize ground-based data sources because a long time series from a single location allows for accurate removal of background climate. The disadvantage of ground-based wind data is that observations are restricted to nighttime. The only previous study to compare GITM to ground-based thermospheric data sources is Liuzzo et al. (2015), which analyzed a case study of the 24 November 2012 substorm using different high-latitude drivers, comparing with the wind observed by Scanning Doppler Imagers at high latitudes. In this paper, we focus on middle and low latitudes. We also restrict our attention to quiet time weather ($K_p \leq 3$) as it is understudied relative to storm time, and quiet conditions dominate the database.

GITM was run using inputs from 2013, and as such, this paper discusses weather during a weak solar maximum. The solar cycle effect on climatological thermospheric winds at middle and low latitudes has been found to be small (0–50 m/s; Dandenault, 2018; Emmert et al., 2006; Fisher et al., 2015). The solar cycle effect on thermospheric weather is not known.

In the following sections, we describe the year-long GITM run, the instrumentation and observations, and our method of calculating the weather. Next, we investigate characteristics of the weather in the model and in the data, and we quantify how well the model is capturing the observed weather.

2. Model

GITM is a global model that describes the upper atmosphere of the Earth and its coupling to the ionosphere from 100-km altitude to approximately 500–600-km altitude, depending on solar activity (Ridley et al., 2006). GITM solves the Navier-Stokes equations for the thermosphere, broken into vertical and horizontal directions. In the vertical direction, a momentum and continuity equation is solved for each species. Coupling terms tie together the constituents in the lower thermosphere, and a bulk vertical wind is calculated given the mass-weighted average of the individual vertical winds. In the horizontal direction, only a bulk momentum equation is solved for, with each species being advected with the bulk wind. For both the horizontal and vertical directions, ion drag, Coriolis, gradient in pressure, and geometric terms are considered. In the horizontal direction, vertical shears are reduced with viscosity. In the vertical momentum equation, viscosity is not considered at this time due to the large horizontal scales for shear in the vertical wind, but gravity is considered.

GITM was run with 4.0° longitude by 2.5° latitude by roughly 0.3 scale height resolution. The altitude spacing in GITM was based on scale heights determined from NRLMSISE-00 (Picone et al., 2002) temperature and mean major mass results for the dayside equator at the start time of each simulation. The time step in GITM was roughly 2 to 3 s and was dynamically set based on the speed of sound, ion and neutral wind speeds, and the size of each cell in all three dimensions. In the majority of cases, the time step was limited due to the smallest altitude spacing and the speed of sound.

The GITM runs were driven by NRLMSISE-00 and Horizontal Wind Model 2014 (Drob et al., 2015) at the lower boundary and Weimer (2005) electric potential patterns and Newell et al. (2014) auroral precipitation patterns at the upper boundary. Both the potential and the aurora were driven by interplanetary

Table 1
Global Ionosphere Thermosphere Model Parameters for the Simulations Presented in This Study

Parameter	Value
Eddy diffusion coefficient	300
Eddy pressure lower	0.005
Eddy pressure upper	0.0005
Photoelectron heating efficiency	0.00
Neutral heating efficiency	0.05
Thermal conduction (molecular)	5.6e-4
Thermal conduction (atomic)	7.6e-4
Thermal conduction power	0.72
AUSMSolver	True
CFL	0.80
Limiter	MC, 2.0
Dynamo high lat. boundary	45.0
Improved ion advection	True
Nighttime ion B.C.s	True
Minimum TEC for Ion B.C.s	2.0
UseTestViscosity	True
TestViscosityFactor	1.0

Note. CFL = Courant-Friedrichs-Lewy condition; B. C. = boundary condition; TEC = total electron content; MC = monitized central—symmetric (van Leer, 1977).

magnetic field and solar wind data. Daily averaged solar irradiance specifications from Flare Irradiance Spectral Model were used. Table 1 specifies the inputs that were used for the simulation. GITM is freely available for download on GitHub.

Because of the time step in GITM and some of the complexities in the chemistry and advection schemes, GITM typically runs roughly 10 times faster than real time at this resolution. This means that in order to run a full year continuously, it would take roughly 37 days. To mitigate this, each month was run individually. This means that GITM was started on the first day of each month and was run for the complete month. The run was allowed to continue into the next month for about 3 days, and the first 3 days of the simulation were swapped for the last 3 days of the previous month's run. For example, for March, the first 3 days of March were deleted for the March run and first 3 days of March were used from the last days of the February run.

A second large run was performed, spanning most of 2013, with higher resolution in the latitudinal direction (1.0° instead of 2.5°). While there were differences in the results, the main conclusions of the study reported here were not altered. We use the lower resolution model here because it covers all of 2013.

3. Instrumentation and Observations

This study uses data from six ground-based Fabry-Perot interferometers (FPIs) at middle and low latitudes in the American sector, as shown in Figure 1. The FPIs make narrow-field-of-view measurements of naturally occurring 630.0-nm airglow, which is emitted in a layer around 250-km altitude. Estimates of the Doppler shift and width of this emission are a measure of the line-of-sight (LoS) thermospheric wind and temperature. The instrument design is described in detail by Meriwether et al. (2011). The six FPIs are organized into two networks: the North American Thermosphere-Ionosphere Observing Network (NATION), described by Makela et al. (2014), and the Remote Equatorial Night-time Observatory of Ionospheric Regions (RENOIR), described by Makela et al. (2013). Although the database includes many years of data, in this paper we use 2013 to match GITM.

These FPIs operate by cycling through a variety of look directions, including occasional observations of a frequency-stabilized laser for calibration. A variety of operating modes were used in 2013, including cardinal

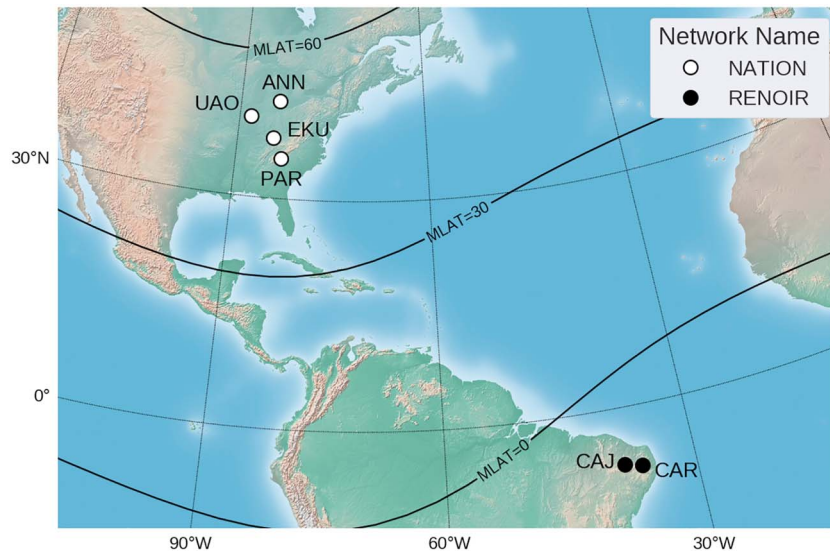


Figure 1. Locations, three-letter site codes, and network names for the six Fabry-Perot interferometer sites used in this study. Magnetic latitude (MLAT) is also shown. NATION = North American Thermosphere-Ionosphere Observing Network; RENOIR = Remote Equatorial Night-time Observatory of Ionospheric Regions

mode (which cycles through north, east, south, and west, at a 45° zenith angle, followed by zenith) and common-volume mode (which optimizes look directions to observe the same location from different sites); see Makela et al. (2013) for more details. In this work, each instrument is analyzed for winds independently. The data set also includes an operational mode with a constant exposure time (usually set to 180, 210, or 300 s) as well as a mode that adjusts the exposure time to maintain a constant measurement uncertainty.

3.1. Analysis

Each observation's raw data are analyzed using the algorithm described by Harding et al. (2014) to obtain LoS wind estimates, which are ascribed to an altitude of 250 km. To convert the various LoS wind observations from a single instrument into an estimate of the zonal and meridional winds, the LoS data are first collected in half hour bins. Half hour bins were chosen to match the GITM samples. The zonal and meridional directions refer to a geographic coordinate system. The unknown zonal wind, u , meridional wind, v , and Doppler reference, Δd , in each bin are fit in the least-squares sense (accounting for measurement uncertainties) to the following observation model:

$$d_i = u \sin \theta_i \sin \varphi_i + v \cos \theta_i \sin \varphi_i + \Delta d, \quad (1)$$

where d_i is the i th LoS wind in the bin, θ_i is the azimuth angle of that measurement, and φ_i is the zenith angle. On average, eight LoS observations contribute to each estimate of u , v , and Δd , though it ranges from 3 to 27. The assumption is that the vertical wind is zero. This differs from the procedure used in previous studies, which allowed for the estimation of time-dependent vertical winds, but which also required an assumption that the average vertical wind over a night is zero (e.g., Makela et al., 2013). In this study, we assume that the instantaneous vertical wind is zero, as this allows Δd to vary. Ideally, the time dependence of Δd is accounted for by frequent laser calibration observations, but allowing Δd to vary better handles nonideal cases such as laser drift, instrument fluctuations that are more rapid than the calibration cadence, and most importantly, contamination by emission lines such as OH which are not addressed by the quality control algorithm (described below). The binned least-squares procedure is general enough to handle data from both cardinal and common-volume modes of operation.

We multiply all horizontal winds by 1.10 to correct for the scattering of airglow in the troposphere, as recommended by Harding et al. (2017). This does not affect any reported correlations, but it reduces the normalized standard deviations in Figure 5. This simple correction is appropriate for cases with no horizontal airglow gradients. In the data set used here, the variation of airglow brightness measured in different directions is on average 28%, so the correction should likely be larger and depend on direction. However, it cannot be evaluated without colocated all-sky imagers at each site and prohibitively expensive computation.

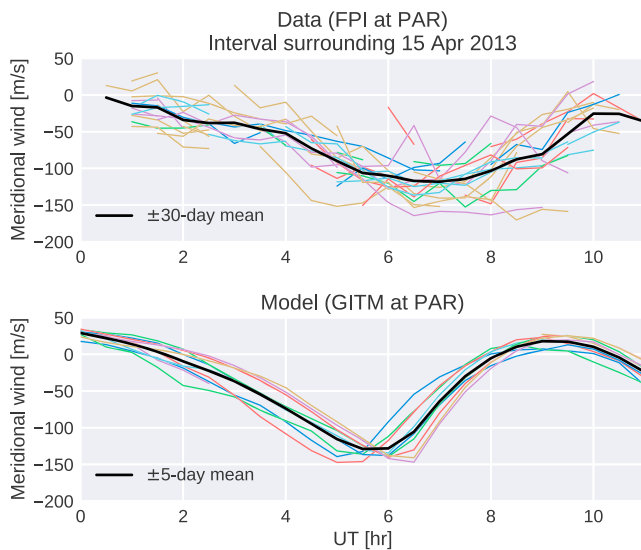


Figure 2. Meridional wind during an interval surrounding 15 April 2013. Thin, colored lines denote the wind from individual nights in the data (top) and model (bottom). An interval of 60 days is shown for the data, while 10 days are shown for the model. The thick black line is the computed background climate. Statistical errors in the data range from 4 to 40 m/s, averaging 12 m/s. FPI = Fabry-Perot interferometer; GITM = Global Ionosphere Thermosphere Model

3.2. Quality Control

The quality control algorithm first removes all LoS measurements with temperatures less than 150 K or uncertainties greater than 100 m/s or 100 K, as these indicate poor raw data quality or poor fringe fitting. Samples for which the continuum background spectrum contribution is more than 0.4 counts per second are considered to be contaminated by moonlight and are removed. It is well known that when the 630.0-nm emission is dim, the nearby OH emissions at 629.8 and 630.7 nm have a contaminating effect upon the winds (Hernandez, 1974; Ronksley, 2016), and the effect depends upon the characteristics of the instrument's interference filter. We remove samples for which the measured brightness is below a predetermined instrument-dependent threshold, chosen by binning historical zenith observations by brightness, and choosing the brightness for which the measured wind deviates from zero by more than 20 m/s.

A second quality control step is implemented after the binning and conversion from LoS to horizontal winds. Bins for which the least-squares fit to equation (1) is deemed untrustworthy (matrix condition number greater than 10, root-mean-square [RMS] residual greater than 50 m/s, or propagated uncertainty greater than 50 m/s) are removed. To focus on quiet times, bins for which the maximum value of K_p in the previous 24 hr is greater than 3 are eliminated. Bins which contain any samples deemed cloudy are removed. Cloud detection is implemented using a colocated Boltwood cloud sensor, which measures the ambient temperature and the infrared sky temperature. When the infrared tem-

perature minus the ambient temperature is greater than a threshold, cloudy conditions are indicated. The best choice for this threshold is not obvious, and some analyses (not shown) have suggested that it may depend on site and season. In the absence of any justification for which functions to use, in this work we use a scalar threshold of -22°C . Although the manufacturer recommends a threshold of -25°C , we find that this results in nearly all summer days at UAO and PAR to be considered cloudy. Although many of the quality control parameters listed above are somewhat arbitrarily chosen, the same qualitative conclusions are reached when other reasonable parameters are used. After quality control, 490–790 hr of data are available per instrument, which represents about 25% of the raw data set.

4. Results and Discussion

We take the modeled and observed horizontal winds for 2013 and first calculate the weather. For the model, the weather at a particular time is defined by subtracting the average wind at the same time of day in ± 5 -day window. Bins which do not contain at least seven samples for defining the climate are removed. For the data, a ± 30 -day window is used. Although ideally the same window length would be used, a shorter window than ± 30 days is not supported by the data density, and if a longer window is used for the model, the resulting weather is dominated by a monthly artifact arising from the model restart, not the true day-to-day variability. The underlying cause of the artifact is unknown but under investigation. Different quantitative results are obtained for different definitions of climate (e.g., a ± 10 -day instead of ± 5 -day window), but the qualitative conclusions are unchanged.

Figure 2 shows observed and modeled meridional winds from an interval surrounding 15 April 2013. Each thin colored line contains data from one night, and the thick black line is the calculated background climate. The weather is defined as the difference. We emphasize that features such as unvarying tidal structures (e.g., diurnal and semidiurnal) would not be included in the following analysis, since they would be subtracted as part of the climate. It is only the day-to-day variations in these tides that would be considered weather in this study. In the following sections, we answer the questions: when there is a disturbance from the background climate, how long does it last, how widespread is it, and how well does the model capture the disturbance?

4.1. Decorrelation Time

To quantify the temporal persistence of the weather, we calculate its autocorrelation function. An example for the CAR zonal wind is shown in the left panel of Figure 3. The correlation decreases with increasing

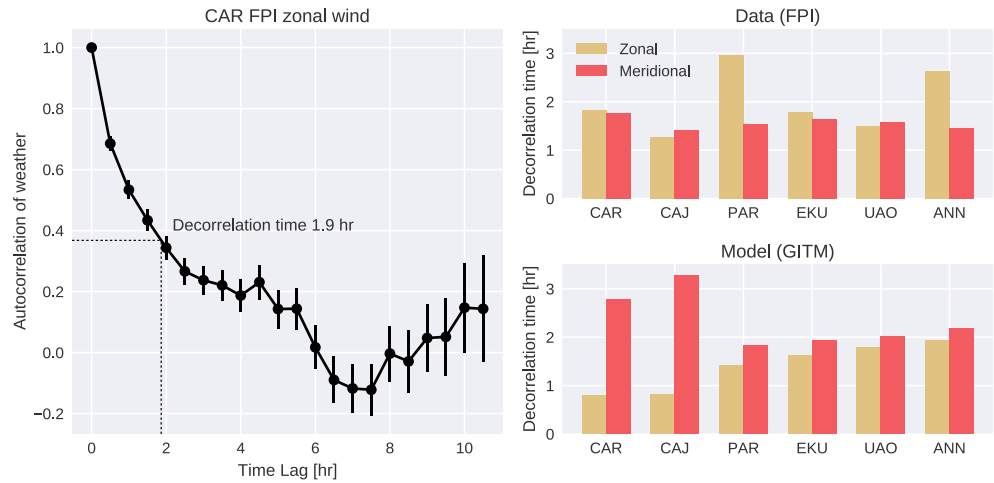


Figure 3. (Left) The measured time-lagged autocorrelation function for the CAR zonal wind weather, with the computed decorrelation time. (Right) The decorrelation time at all sites in both the zonal and meridional wind for the data (top) and model (bottom). FPI = Fabry-Perot interferometer; GITM = Global Ionosphere Thermosphere Model

time lag, and the time lag at which the correlation drops to e^{-1} is 1.9 hr. We refer to this as the decorrelation time. Past this time delay, the fluctuations about the background climate can be considered uncorrelated.

The right panel of Figure 3 displays the decorrelation times for the zonal and meridional winds at all sites, in both the data and the model. On average, the model and the data agree remarkably well, with decorrelation times of 1.9 and 1.8 hr, respectively. In the model, at midlatitudes (PAR, EKU, UAO, and ANN), zonal and meridional decorrelation times are nearly identical, yet at low latitudes (CAR and CAJ), the zonal decorrelation time is much shorter. No evidence for this is seen in the data, for which the zonal and meridional decorrelation times are similar at all sites, except for the PAR and ANN zonal wind, which are larger. ANN and PAR are the northernmost and southernmost sites in the midlatitude network, so there does not appear to be any physical reason why their decorrelation times are the longest.

4.2. Decorrelation Distance

To quantify the spatial scale spanned by structures in the weather, we compute the cross-correlation between sites. In comparing the model results with the data, we must take care to account for noise in the data. For example, if two sites observe exactly the same weather but encounter different noise, the correlation is less than one. Assuming the propagated uncertainties are correctly estimated, this effect can be corrected by using a modified cross-correlation. The standard Pearson correlation coefficient between two measurements y_1 and y_2 can be written as

$$\rho = \frac{\langle y_1 y_2 \rangle}{\sqrt{\langle y_1^2 \rangle} \sqrt{\langle y_2^2 \rangle}}, \quad (2)$$

where $\langle \cdot \rangle$ denotes ensemble or temporal average. In the case where the measurement is a combination of signal and noise ($y = s + n$), the noise is uncorrelated with the signal, the noise is uncorrelated between sites, and the noise power $\langle n^2 \rangle$ is known, the modified correlation coefficient can be calculated as

$$\rho' = \frac{\langle y_1 y_2 \rangle}{\sqrt{\langle y_1^2 \rangle - \langle n_1^2 \rangle} \sqrt{\langle y_2^2 \rangle - \langle n_2^2 \rangle}}. \quad (3)$$

For this data set, ρ' is larger than ρ by about 10–20%.

Figure 4 shows the modified cross-correlations for all pairs of sites, as a function of baseline (i.e., great-circle distance between the sites). In general, the trend is smaller correlations for longer baselines, with correlations over the long distances between NATION and RENOIR near zero. The modeled weather has much higher correlation than the data, suggesting that the model is smoothing over spatial structure that is observed in real weather.

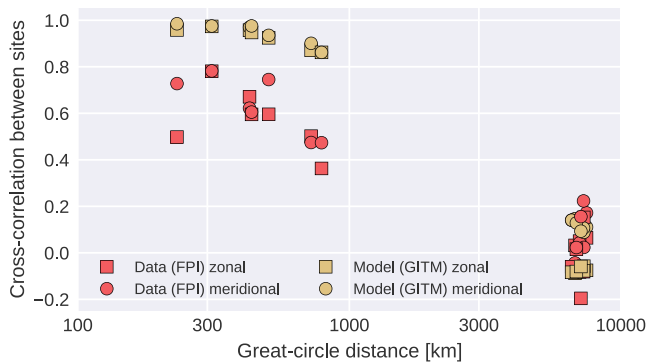


Figure 4. Cross-correlations for all pairs of sites, for both the zonal and meridional wind in the data and the model. FPI = Fabry-Perot interferometer; GITM = Global Ionosphere Thermosphere Model

Without longer baselines than those available within RENOIR or within NATION, it is impossible to conclusively evaluate the decorrelation distance (the baseline at which the cross-correlation drops to e^{-1}). Nevertheless, upon extrapolation, the data suggest a decorrelation distance of roughly 1,000 km.

The closest baseline is CAJ-CAR at 232 km. While the CAJ-CAR meridional correlation (0.73) fits the general trend well, the low zonal correlation (0.50) appears to be an outlier. Despite much effort, no explanation is apparent, but we suspect that this is caused by a cloud detection problem. This would explain why the zonal wind is affected more than the meridional wind. The zonal wind is generally larger, and the presence of clouds brings the measured wind toward zero. Cloud cover at CAJ but not CAR would cause large differences in the zonal wind. However, the correlation is low for a variety of cloud detection thresholds, as well as seasonally dependent thresholds, so the cause of this low correlation remains unknown.

If the weather were dominated by day-to-day tidal variability, the decorrelation distance would be expected to take on global scales larger than 1,000 km. Combined with the relatively short decorrelation times reported above, this suggests that the weather in the thermosphere is dominated by some other source than tidal variability, possibly large-scale gravity waves generated by high-latitude heating (often called traveling atmospheric disturbances).

It should be noted that the estimates of $\langle n_1^2 \rangle$ and $\langle n_2^2 \rangle$ used in (3) contain statistical noise only. Systematic errors can arise as a consequence of OH contamination, atmospheric scattering, rapid ambient temperature changes, and uncertainty in the layer altitude, among other sources. However, the quantification of these errors is too uncertain to include in this analysis. If they were included, they would increase the correlations shown in Figure 4, but it is unlikely they would change the conclusion that the decorrelation distance is less than tidal scales.

A caveat of this analysis is that the wind estimate uses oblique measurements, which sample the thermosphere at locations horizontally removed from the site location. For example, in cardinal mode, the pierce points of the north-, east-, south-, and west-observing directions are 250 km away. Because of this, the true cross-correlations for baselines less than about 500 km are likely lower than reported here.

One might expect that given the relatively short decorrelation times and distances, weather may arrive at different sites at different times. To address this, we performed a time-lag analysis. The time-lagged cross-correlation functions are broad (1–3 hr) and peaked at or near zero, so adding a time lag does not significantly change the results shown in Figure 4.

4.3. Model-Data Correlation

The previous two subsections compared the statistics of the modeled weather with the statistics of the observed weather. This section quantifies how well the weather compares on a day-to-day basis. To evaluate GITM's performance in capturing the weather, we use Taylor diagrams (Taylor, 2001), which have previously been applied to space physics by Elvidge et al. (2014). Taylor diagrams combine two commonly used metrics for model performance, correlation and RMS error, using the fact that their relationship resembles the law of cosines.

The Taylor diagrams for GITM's zonal and meridional weather are shown in Figure 5. Each is a polar plot where the angle is arccosine of the model-data correlation, which is calculated including a modification like in (3) to account for noise in the data. The radius is the standard deviation of the modeled weather, divided by the standard deviation of the observed weather. Again, a correction is included to remove the noise power. The dashed contours are RMS error, normalized to the standard deviation of the observed weather. A perfect model with zero error is located at the lower right corner, with a correlation of 1.0 and a normalized standard deviation of 1.0.

Immediately evident in Figure 5 is the large RMS error of ~ 1.0 , indicating that the model error is of the same magnitude as the observed weather. The model error is understood in terms of two sources. First, the modeled weather is too small, with a normalized standard deviation of 0.35 on average, indicating that

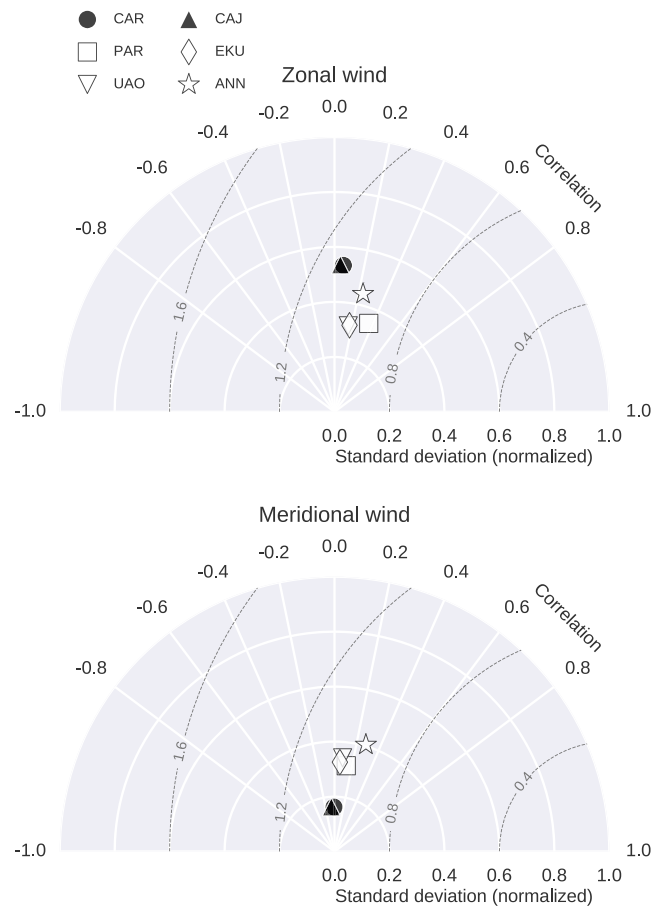


Figure 5. Taylor diagrams evaluating the model performance in the zonal (top) and meridional (bottom) weather. The angular coordinate represents model-data correlation, and the radial coordinate represents modeled weather standard deviation divided by observed weather standard deviation. The root-mean-square error can be calculated from these two values and is shown in dashed contours

the magnitude of the weather is underestimated by 65% in the model. The low latitude meridional wind fluctuations are particularly underestimated in the model (0.16). Second, the correlations are low, ranging from -0.07 to 0.36 . The uncertainty in the reported correlations is ~ 0.03 . In general, for both the zonal and meridional wind, the low latitude correlations (insignificantly different from zero) are less than the midlatitude correlations (0.19 on average). The midlatitude correlations are small yet statistically significant, indicating that while GITM's performance in capturing the weather is quite poor, it is at least representing some of the relevant physics at midlatitudes. This is perhaps surprising given the relative simplicity of the lower-boundary and high-latitude forcing in the model. Especially at low latitudes, the performance may be improved by including data-driven lower boundary tidal variability, but the short decorrelation distances and times in the data suggest this would not address the dominant type of weather.

Unlike the previous results, which were based on correlations, the standard deviations are sensitive to the assumed emission altitude of 250 km. A sensitivity test was performed in which the winds were extracted from the model at two other altitudes, 210 and 290 km. The normalized standard deviations were 25–50% lower at 210 km compared to 290 km, indicating that the magnitude of the weather is larger at higher altitudes. However, using a different altitude than 250 km does not change the conclusion that the magnitude of the weather is underestimated in the model.

5. Conclusion

We have presented the first long-term comparison of thermospheric weather between a first-principles numerical model and data. Using nighttime thermospheric wind data from 2013 at six FPI sites at middle and low latitudes, we have characterized fluctuations about the climate during quiet times, focusing on three

questions: how long do fluctuations last, how widespread are they, and how well does the model reproduce the observed weather? The data indicate an average decorrelation time of 1.8 hr and suggest a decorrelation distance of about 1,000 km. The weather in the model (GITM) has a remarkably similar decorrelation time of 1.9 hr, but nearby sites are much more correlated than in the data, suggesting that the modeled weather is too smooth spatially but has the correct temporal persistence. The short decorrelation time and distance in the data suggest that the dominant mode of variability is not tidal.

The model's ability to capture day-to-day variations in the weather is poor. It underestimates the magnitude of the weather by 65%. Averaged between the zonal and meridional winds, model-data correlations are near zero at low latitudes and 0.19 at midlatitudes. Clearly, much work remains to model thermospheric weather, and our work suggests that focusing on high-latitude drivers is likely to be more successful than improving lower boundary tidal forcing.

These results could be useful for assimilative models, at least for the regions studied here (middle and low latitudes in the American sector). Most assimilative models have a notion of model covariance, which characterizes the temporal and spatial scales over which incoming measurements should inform the next estimate. The reported decorrelation time and distance could help tune model covariance, as there is a clear analogy between our definition of weather and the innovation sequence used in Kalman filters.

The site-to-site cross-correlations in Figure 4 reveal a significant gap in our understanding of the weather on scale sizes between 790 km (the longest baseline in NATION) and ~7,000 km (the distance between NATION and RENOIR). They also suggest that the NATION FPIs are not optimally distributed. For example, the EKV-PAR correlation (baseline 311 km) is 0.78, so most of the information would have been captured by just one site. If the goal is to maximize the observability of fluctuations in the thermospheric wind, future deployments should target longer baselines.

Acknowledgments

The FPI data in this work are available on the Madrigal database or can be made available by request. The Kp data used were obtained from the National Oceanic and Atmospheric Administration's National Centers for Environmental Information. Work at the University of Illinois was supported by NSF grant AGS 14-52291. The authors recognize the NATION and RENOIR teams for support hosting and maintaining the instruments. At the University of Michigan, the research was supported through the NSF grant ATM-1452097 and AFOSR under DDDAS (Dynamic Data-Driven Applications Systems, <http://www.1dddas.org/>) grant FA9550-16-1-0071. The simulations were conducted on NASA Pleiades.

References

- Dandena, P. B. (2018). MENTAT: A new wind model for Earth's thermosphere. *Journal of Geophysical Research: Space Physics*, *123*, 7124–7147. <https://doi.org/10.1029/2018JA025551>
- Deng, Y., & Ridley, A. J. (2006). Dependence of neutral winds on convection E-field, solar EUV, and auroral particle precipitation at high latitudes. *Journal of Geophysical Research*, *111*, A09306. <https://doi.org/10.1029/2005JA011368>
- Drob, D. P., Emmert, J. T., Meriwether, J. W., Makela, J. J., Doornbos, E., Conde, M. G., et al. (2015). An update to the Horizontal Wind Model (HWM): The quiet time thermosphere. *Earth and Space Science*, *2*, 301–319. <https://doi.org/10.1002/2014EA000089>
- Elvidge, S., Angling, M. J., & Nava, B. (2014). On the use of modified Taylor diagrams to compare ionospheric assimilation models. *Radio Science*, *49*, 737–745. <https://doi.org/10.1002/2014RS005435>
- Emmert, J. T., Faivre, M. L., Hernandez, G., Jarvis, M. J., Meriwether, J. W., Niciejewski, R. J., et al. (2006). Climatologies of nighttime upper thermospheric winds measured by ground-based Fabry-Perot interferometers during geomagnetically quiet conditions: 1. Local time, latitudinal, seasonal, and solar cycle dependence. *Journal of Geophysical Research*, *111*, A12302. <https://doi.org/10.1029/2006JA011948>
- Emmert, J. T., Fejer, B. G., Fesen, C. G., Shepherd, G. G., & Solheim, B. H. (2001). Climatology of middle- and low-latitude daytime F region disturbance neutral winds measured by Wind Imaging Interferometer (WINDII). *Journal of Geophysical Research*, *106*(A11), 24,701–24,712. <https://doi.org/10.1029/2000JA000372>
- Fisher, D. J., Makela, J. J., Meriwether, J. W., Buriti, R. A., Benkhalidoun, Z., Kaab, M., & Lagheryeb, A. (2015). Climatologies of nighttime thermospheric winds and temperatures from Fabry-Perot interferometer measurements: From solar minimum to solar maximum. *Journal of Geophysical Research: Space Physics*, *120*, 6679–6693. <https://doi.org/10.1002/2015JA021170>
- Harding, B. J., Gehrels, T. W., & Makela, J. J. (2014). Nonlinear regression method for estimating neutral wind and temperature from Fabry-Perot interferometer data. *Applied Optics*, *53*(4), 666. <https://doi.org/10.1364/AO.53.000666>
- Harding, B. J., Qin, J., & Makela, J. J. (2017). Ground-based optical measurements of quiet time thermospheric wind and temperature: Atmospheric scattering corrections. *Journal of Geophysical Research: Space Physics*, *122*, 11,624–11,632. <https://doi.org/10.1002/2017JA024705>
- Hernandez, G. (1974). Contamination of the OI(3P2-1D2) emission line by the (9-3) band of OH X2II in high-resolution measurements of the night sky. *Journal of Geophysical Research*, *79*(7), 1119–1123. <https://doi.org/10.1029/JA079i007p01119>
- Liuzzo, L. R., Ridley, A. J., Perlongo, N. J., Mitchell, E. J., Conde, M., Hampton, D. L., et al. (2015). High-latitude ionospheric drivers and their effects on wind patterns in the thermosphere. *Journal of Geophysical Research: Space Physics*, *120*, 715–735. <https://doi.org/10.1002/2014JA020553>
- Makela, J. J., Fisher, D. J., Meriwether, J. W., Buriti, R. A., & Medeiros, A. F. (2013). Near-continual ground-based nighttime observations of the thermospheric neutral winds and temperatures over equatorial Brazil from 2009 to 2012. *Journal of Atmospheric and Solar-Terrestrial Physics*, *103*, 94–102. <https://doi.org/10.1016/j.jastp.2012.11.019>
- Makela, J. J., Harding, B. J., Meriwether, J. W., Mesquita, R., Sanders, S., Ridley, A. J., et al. (2014). Storm time response of the midlatitude thermosphere: Observations from a network of Fabry-Perot interferometers. *Journal of Geophysical Research: Space Physics*, *119*, 6758–6773. <https://doi.org/10.1002/2014JA019832>
- Mehta, P. M., Walker, A. C., Sutton, E. K., & Godinez, H. C. (2017). New density estimates derived using accelerometers on board the CHAMP and GRACE satellites. *Space Weather*, *15*, 558–576. <https://doi.org/10.1002/2016SW001562>
- Meriwether, J. W., Makela, J. J., Fisher, D. J., Buriti, R., Medeiros, A. F., Akmaev, R., et al. (2013). Comparisons of thermospheric wind and temperature measurements in equatorial Brazil to Whole Atmosphere Model Predictions. *Journal of Atmospheric and Solar-Terrestrial Physics*, *103*, 103–112. <https://doi.org/10.1016/j.jastp.2013.04.002>

- Meriwether, J. W., Makela, J. J., Huang, Y., Fisher, D. J., Buriti, R. A., Medeiros, A. F., & Takahashi, H. (2011). Climatology of the nighttime equatorial thermospheric winds and temperatures over Brazil near solar minimum. *Journal of Geophysical Research*, *116*, A04322. <https://doi.org/10.1029/2011JA016477>
- Newell, P. T., Liou, K., Zhang, Y., Sotirelis, T., Paxton, L. J., & Mitchell, E. J. (2014). OVATION Prime-2013: Extension of auroral precipitation model to higher disturbance levels. *Space Weather*, *12*, 368–379. <https://doi.org/10.1002/2014SW001056>
- Picone, J. M., Hedin, A. E., Drob, D. P., & Aikin, A. C. (2002). NRLMSISE-00 empirical model of the atmosphere: Statistical comparisons and scientific issues. *Journal of Geophysical Research*, *107*(A12), 1468. <https://doi.org/10.1029/2002JA009430>
- Ridley, A., Deng, Y., & Toth, G. (2006). The global ionosphere-thermosphere model. *Journal of Atmospheric and Solar-Terrestrial Physics*, *68*(8), 839–864. <https://doi.org/10.1016/j.jastp.2006.01.008>
- Ronksley, A. (2016). Optical remote sensing of mesoscale thermospheric dynamics above Svalbard and Kiruna, (PhD thesis). University of London.
- Sutton, E. K., Nerem, R. S., & Forbes, J. M. (2007). Density and winds in the thermosphere deduced from accelerometer data. *Journal of Spacecraft and Rockets*, *44*(6), 1210–1219. <https://doi.org/10.2514/1.28641>
- Taylor, K. E. (2001). Summarizing multiple aspects of model performance in a single diagram. *Journal of Geophysical Research*, *106*(D7), 7183–7192. <https://doi.org/10.1029/2000JD900719>
- Van Leer, B. (1977). Towards the ultimate conservative difference scheme. III. Upstream-centered finite-difference schemes for ideal compressible flow. *Journal of Computational Physics*, *23*(3), 263–275. [https://doi.org/10.1016/0021-9991\(77\)90094-8](https://doi.org/10.1016/0021-9991(77)90094-8)
- Weimer, D. R. (2005). Improved ionospheric electrodynamic models and application to calculating joule heating rates. *Journal of Geophysical Research*, *110*, A05306. <https://doi.org/10.1029/2004JA010884>
- Wu, Q., Emery, B. A., Shepherd, S. G., Ruohoniemi, J. M., Frissell, N. A., & Semeter, J. (2015). High-latitude thermospheric wind observations and simulations with SuperDARN data driven NCAR TIEGCM during the December 2006 magnetic storm. *Journal of Geophysical Research: Space Physics*, *120*, 6021–6028. <https://doi.org/10.1002/2015JA021026>
- Wu, Q., McEwen, D., Guo, W., Nijcejewski, R., Roble, R., & Won, Y.-I. (2008). Long-term thermospheric neutral wind observations over the northern polar cap. *Journal of Atmospheric and Solar-Terrestrial Physics*, *70*(16), 2014–2030. <https://doi.org/10.1016/j.jastp.2008.09.004>